

Numerical analysis of real gas MHD flow on two-dimensional self-field MPD thrusters



Carlos M. Xisto*, José C. Páscoa, Paulo J. Oliveira

Departamento de Engenharia Electromecânica, Universidade da Beira Interior, C-MAST: Center for Mechanical and Aerospace Sciences and Technologies, FCT Research Unit No. 151, Covilhã 6201-001, Portugal

ARTICLE INFO

Article history:

Received 11 September 2014

Received in revised form

7 February 2015

Accepted 6 March 2015

Available online 14 March 2015

Keywords:

MHD

AUSM-MHD

MHD

PISO

Self-field MPD

Real-gas

ABSTRACT

A self-field magnetoplasmadynamic (MPD) thruster is a low-thrust electric propulsion space-system that enables the usage of magnetohydrodynamic (MHD) principles for accelerating a plasma flow towards high speed exhaust velocities. It can produce an high specific impulse, making it suitable for long duration interplanetary space missions. In this paper numerical results obtained with a new code, which is being developed at C-MAST (Centre for Mechanical and Aerospace Technologies), for a two-dimensional self-field MPD thruster are presented. The numerical model is based on the macroscopic MHD equations for compressible and electrically resistive flow and is able to predict the two most important thrust mechanisms that are associated with this kind of propulsion system, namely the thermal thrust and the electromagnetic thrust. Moreover, due to the range of very high temperatures that could occur during the operation of the MPD, it also includes a real gas model for argon.

© 2015 IAA. Published by Elsevier Ltd. All rights reserved.

1. Introduction

Low-thrust electric propulsion systems are being developed for long duration space missions [1] and station keeping [2]. In classical chemical propulsion devices, thrust is a product of an exothermic process of combustion. By using an electrical propulsion system, it is possible to decouple the achievable exhaust speed from the amount of energy produced by the reaction. Therefore, the specific impulse achievable via electrically-based thrusters is as high as the amount of energy one can put into the exhaust, which uniquely depends on the technology level. Among the electrical propulsion systems, the MPD (magnetoplasmadynamic) thruster is capable of delivering one of the highest thrust densities [3,4]: e.g.

the DT2-IRS self-field thruster is capable of providing a thrust density of around 3565 N/m^2 [5]. There are several parameters that need to be considered during the development of an electric propulsion device, namely optimal exhaust velocity; generator specific power; mission duration; and total impulse. All of these need to be properly related. The optimal exhaust velocity is determined by the generator specific power, by the duration of the mission and by the necessary total impulse to fulfil such mission [6].

Fig. 1 shows a planar (a) and a co-axial (b) self-field MPD thruster. In a simplified form the co-axial device can be represented by a central cathode surrounded by a concentric anode [7]. Both surfaces will define a chamber that will accommodate a discharge current of several kA. Afterwards, the propellant is injected and the interaction between the self-generated azimuthal magnetic field and the radial and axial components of the discharge current will generate processes of acceleration. MPD thrusters can also be categorized by different regimes of

* Corresponding author.

E-mail addresses: xisto@ubi.pt (C.M. Xisto), pascoa@ubi.pt (J.C. Páscoa), pjpo@ubi.pt (P.J. Oliveira).

electromagnetic interaction. In self-field MPD nozzles the only available component of the magnetic field is the self-induced one, and its interaction with the discharge current will give rise to axial ($j_r B_\theta$) and radial ($-j_z B_\theta$) components of the Lorentz force ($F_{ELM} = \mathbf{j} \times \mathbf{B}$). In applied-field thrusters, there is an extra magnetic field that is imposed by an external coil and its radial and axial components will interact with the discharge current in order to stabilize and accelerate the plasma flow [8]. In both devices the high temperature that is triggered by the Joule heating effect will result in an electro-thermal component of thrust.

The usage of MPD thrusters in a regular basis for space propulsion or satellite reposition is being consecutively delayed because of their relatively low efficiency for the relevant regimes of operation. The highest efficiency recorded for an MPD nozzle was 69% for a specific impulse of 5500 s with a power consumption of 20 kW [9]. However the most efficient regime of operation lies between 200 kW and 500 kW. For a power value closer to these ones (100 kW) the highest value for efficiency (50%) was recorded by [10] while using vaporized lithium as a propellant. However, one knows that vaporized lithium normally leads to condensation problems that may damage the surface of the spacecraft [7]. Argon or hydrogen can also be considered with a cost of reducing the efficiency. Nevertheless, several studies show

that the efficiency is improved, not just by selecting a propellant with better electrical properties [11], but also by modifying the geometry of the electrodes [12,13], or by imposing an externally generated magnetic field [14].

The numerical modeling of MPD thrusters is an important tool for analysing the complex interaction between the flow of a conducting gas and the applied and/or induced magnetic fields. Several codes with different levels of complexity were introduced for analysing self-field coaxial MPD thrusters. Models were developed assuming a two-dimensional axisymmetrical approximation [12,15–19], while others were applied for computing bi-dimensional geometries using pure 2D cartesian formulations [20,21,11]. Extensions of the previous models for solving the plasma flow in applied-field MPD thrusters have also been proposed in the subsequent years [14,22,8]. The earlier attempts assumed that the plasma flow could be approximated by a one-fluid model [23,20]. Such assumption leads to errors in the prediction of plasma transport coefficients, since these need to be defined in different ways for the electrons, ions and neutral species [24]. Others have considered a one-fluid approach but have assumed a thermal non-equilibrium between species [12,15,16,25]. Nevertheless, a single fluid model like the one here proposed is still useful for a better understanding of the main acceleration mechanisms that are generated by this kind of systems [26].

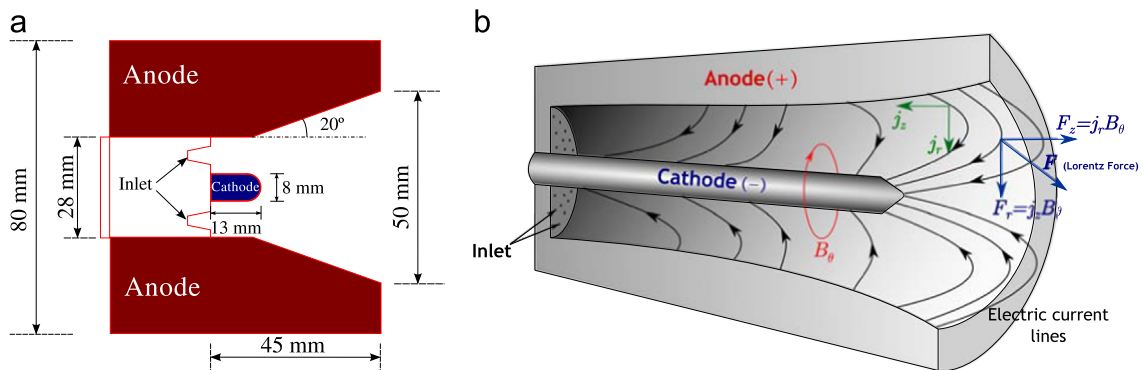


Fig. 1. Representation of two different types of magnetoplasmadynamic thrusters. (a) Two-dimensional MPD; (b) co-axial MPD.

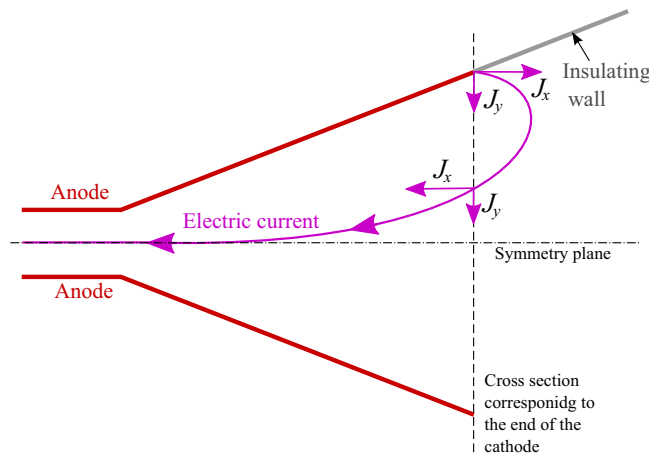


Fig. 2. Two-dimensional representation of the discharge current and its interaction with the anode and the insulating walls.

In the current paper, results obtained with a plasma dynamic numerical code that is being developed at C-MAST (Centre for Mechanical and Aerospace Technology), for solving three-dimensional flows on MPD thrusters, are presented and discussed. In the current state of development, the model considers the plasma as a continuum medium in a state of total ionization, and thermal equilibrium between species is assumed. In this way a single system of conservation laws is to be solved and we will also assume a single temperature for the plasma. These assumptions will lead to some discrepancies between the computed and the real transport properties. The effects of radiation, ion slip, Hall effect, and anomalous transport will also be neglected during this phase of code development. That said, the model here presented allows us to analyse with some detail the main acceleration mechanisms present in MPD thrusters. We have also included a real gas model for argon, based on partition functions [27,28], which will be adapted into the current numerical framework so as to allow for a more realistic solution of plasma temperature. The model also employs one of the most recent and accurate flux schemes [29] for computing MHD discontinuities, and can cope with plasma flows at arbitrary Mach numbers [30], one feature that was missing from the previous formulations.

In the next section, the set of equations that govern resistive MHD flow are presented. Afterwards, in Section 3, the numerical model is briefly described and the plasma parameters here analyzed are highlighted. That section is closed with the formulation employed for the real gas model. In Section 4 the numerical method is applied to the computation of the two-dimensional self-field MPD thruster flows. Here the effects due to the geometry of the anode and the cathode, and the influence of mass flow rate are analysed.

2. Magnetohydrodynamics

If the most recent conjectures about the existence of dark matter in the interstellar space are ignored, one can assume that the Universe is essentially composed by plasma. A brief definition of plasma states that it is a gas that has suffered a process of ionization, thus guaranteeing that will be mostly composed by particles of negative charge (electrons) and particles of positive or negative charge (ions). If one assumes a state of total ionization, the presence of neutral charge particles can be neglected and the plasma thus becomes an excellent conductor of electricity. Electric and magnetic fields exist with some abundance in space, therefore one is led to believe that much of the plasma dynamics that occurs in the Universe is due to its interaction with those same fields. As an example, we refer the Earth magnetic field and its interaction with the solar winds [31].

MHD is the field of physics that studies the interaction between magnetic fields and electrically conducting fluids. Such a statement indicates that the MHD macroscopical approximation might be an excellent approach for studying the physics of plasma flow. However, such a statement is not entirely correct since, from a microscopic point of view, a plasma cannot be considered as a continuum

medium. Still, there are additional assumptions that guarantee the applicability of MHD in the description of plasma flow. It is imperative that the reference length scale of the plasma be much larger than the diameter of the volume where the positive and negative charges cancel each other; this volume is known as Debye sphere. The temporal length scale of interest should also be much larger than the collision time between ions, meaning that the collisions between particles have reach a steady state and do not influence the main flow. These assumptions are normally valid for most of the plasma flow in laboratorial scale, in the field of astrophysics [32] and in most of the working regimes of MPD thrusters [6].

The MHD equations couple the magnetic field, given by Maxwell equations, with the flow of a conducting fluid, ruled by the Navier–Stokes equations. The resistive form of the MHD system of equations is given by

$$\frac{\partial \rho}{\partial t} + \nabla \cdot (\rho \mathbf{U}) = 0, \quad (1)$$

$$\frac{\partial \rho \mathbf{U}}{\partial t} + \nabla \cdot \left[\rho \mathbf{U} \mathbf{U} + \left(p + \frac{\mathbf{B} \cdot \mathbf{B}}{2\mu_0} \right) \mathbf{I} - \frac{\mathbf{B} \mathbf{B}}{\mu_0} \right] = \nabla \cdot \boldsymbol{\tau}_{\text{visc}}, \quad (2)$$

$$\frac{\partial \rho e_t}{\partial t} + \nabla \cdot \left[\left(\rho e_t + p + \frac{\mathbf{B} \cdot \mathbf{B}}{2\mu_0} \right) \mathbf{U} - \mathbf{U} \cdot \frac{\mathbf{B} \mathbf{B}}{\mu_0} \right] = \nabla \cdot \left(\frac{\mathbf{B} \times \boldsymbol{\eta} \mathbf{j}}{\mu_0} + \boldsymbol{\tau}_{\text{visc}} \cdot \mathbf{U} \right), \quad (3)$$

$$\frac{\partial \mathbf{B}}{\partial t} + \nabla \cdot (\mathbf{U} \mathbf{B} - \mathbf{B} \mathbf{U}) = -\nabla \times (\boldsymbol{\eta} \mathbf{j}), \quad (4)$$

where $\eta = 1/\sigma$ represents the plasma electric resistivity, μ_0 is the permeability of free space and the electrical current density is \mathbf{j} . This system expresses the conservation of mass (1), momentum (2), total energy (3), and propagation of the magnetic field (4). The viscous stress tensor for compressible newtonian flow is given by

$$\boldsymbol{\tau}_{\text{visc}} = -\left(\frac{2}{3}\mu \nabla \cdot \mathbf{U}\right) \mathbf{I} + \mu \left[\nabla \mathbf{U} + (\nabla \mathbf{U})^T \right], \quad (5)$$

where μ is the dynamic viscosity of the plasma. Temperature is a derived quantity and can be obtained from an equation of state:

$$T = \frac{1}{c_v} \left[e_t - \frac{1}{2} \left(U^2 + \frac{B^2}{\rho \mu_0} \right) \right]. \quad (6)$$

Using Ampère's law and some standard vector identities, the last term of Eq. (4) can be re-written in terms of \mathbf{B} :

$$\nabla \times (\boldsymbol{\eta} \mathbf{j}) = \nabla \times \left(\boldsymbol{\eta} \frac{\nabla \times \mathbf{B}}{\mu_0} \right) = -\nabla \cdot \left(\boldsymbol{\eta} \nabla \frac{\mathbf{B}}{\mu_0} \right). \quad (7)$$

The electrical conductivity is computed as a scalar field formulated using the Spitzer–Harm approximation:

$$\sigma = 1.53 \times 10^{-2} \frac{T^{3/2}}{\ln \Lambda}, \quad (8)$$

where

$$\ln \Lambda = \ln \left(\frac{12\sqrt{2}\pi(k_B \epsilon_0 T)^{3/2}}{q^3 n^{1/2}} \right), \quad (9)$$

is the Coulomb logarithm. In Eq. (9) k_B is the Boltzmann constant, q is related to electron particle charge, ϵ_0 is the

permittivity of free space and n is the particle number density expressed in particles per cubic meter of plasma.

3. Numerical model

The numerical method that is going to be used throughout this paper was developed and validated for the ideal MHD equations by Xisto et al. [33] and for the resistive MHD equations by [34]. This method is based on the PISO algorithm of Issa [35] which was previously modified to solve arbitrary Mach number flows by Xisto et al. [30]. In order to improve accuracy and stability in the computation of the various types of MHD discontinuities, the AUSM-MHD [29] flux scheme was adapted into the current numerical method. The AUSM-MHD method is an improved version of the AUSMPW scheme [36] for ideal MHD, where the pressure-based weight functions were adapted in order to account for the magnetic pressure. For variable interpolation a high resolution scheme, namely the CUBISTA of Alves et al. [37] was used. In multidimensional MHD cases one must ensure $\nabla \cdot \mathbf{B} = 0$ and for that purpose the hyperbolic/parabolic divergence cleaning technique proposed by Dedner et al. [38] was incorporated in the present model.

The code was developed within the Open Field Operation And Manipulation (OpenFOAM) CFD package. The OpenFOAM package is an object-oriented numerical simulation toolkit for continuum mechanics written in C++ language and is currently released by ESI Group.

3.1. Description of the algorithm

The method employs a segregated approach, whereby the system of equations is solved in a sequential way. Therefore in order to couple the dependent variables there is the need to select an appropriate algorithm. Since many of the MHD flows are time-dependent by nature the PISO algorithm was selected. The iterative procedure consists of successive prediction and correction steps, with values obtained at a previous time step denoted with n , and consecutive predictions and corrections denoted with * , ** , *** . In the following subsections units for \mathbf{B} were chosen such that $\mu_0 = 1$ H/m. The convective fluxes are calculated with the AUSM-MHD method using the appropriate characteristic speed, $U \pm c$. The common fast magnetosonic speed is given by

$$c_f = \min(c_L, c_R), \quad (10)$$

where

$$c_{L,R} = \left\{ \frac{1}{2} \left[a_{L,R}^2 + \frac{B_{L,R}^2}{\rho_{L,R}} + \sqrt{\left(a_{L,R}^2 + \frac{B_{L,R}^2}{\rho_{L,R}} \right)^2 - 4a_{L,R}^2 \frac{B_{n,L,R}^2}{\rho_{L,R}}} \right] \right\}^{1/2}. \quad (11)$$

In Eq. (11) $a_{L,R}$ are the left and right states for the speed of sound and $B_n = \hat{\mathbf{S}}_f \cdot \mathbf{B}$ is the face normal component of the magnetic field.

3.1.1. Prediction step

In the prediction step the values for the dependent variables are known from the previous time level n . At the beginning of the computation a suitable estimation for those variables should be provided. One starts by calculating the interpolation Mach number functions ($\overline{\mathcal{M}}_4^\pm$, $\overline{\mathcal{P}}_5^\pm$), which allows the assembling of the flux vectors for the three-dimensional MHD equations (see [34] for more details):

$$\frac{\partial \mathcal{H}}{\partial t} + \nabla \cdot \mathcal{F}_f = \mathcal{S}. \quad (12)$$

In Eq. (12) \mathcal{H} is the state vector for the conservative variables, the flux vectors for the multidimensional MHD equations are given by \mathcal{F}_f and \mathcal{S} , which are the diffusion and source term contributions, respectively. These are given by

$$\mathcal{H} = \begin{pmatrix} \rho \\ \rho U_x \\ \rho U_y \\ \rho U_z \\ B_x \\ B_y \\ B_z \\ \rho e_t \\ \Psi \end{pmatrix}, \quad \mathcal{S} = \begin{pmatrix} 0 \\ \nabla \cdot (\tau_{xx}, \tau_{yx}, \tau_{zx}) \\ \nabla \cdot (\tau_{xy}, \tau_{yy}, \tau_{zy}) \\ \nabla \cdot (\tau_{xz}, \tau_{yz}, \tau_{zz}) \\ \nabla \cdot (\eta \nabla B_x) \\ \nabla \cdot (\eta \nabla B_y) \\ \nabla \cdot (\eta \nabla B_z) \\ \nabla \cdot (\mathbf{B} \times \eta \nabla \times \mathbf{B} + \tau_{\text{visc}} \cdot \mathbf{U}) \\ -\frac{c_h^2}{c_d} \Psi \end{pmatrix}, \quad (13)$$

$$\mathcal{F}_f = c_f \left(\overline{\mathcal{M}}_4^+ \Phi_L^n + \overline{\mathcal{M}}_4^- \Phi_R^n \right) + (\overline{\mathcal{P}}_5^+ \mathbf{P}_L^n + \overline{\mathcal{P}}_5^- \mathbf{P}_R^n) + \frac{1}{2} \left(\Phi_{\mathbf{B},L}^n + \Phi_{\mathbf{B},R}^n \right), \quad (14)$$

$$\Phi = \begin{pmatrix} \rho \\ \rho U_x \\ \rho U_y \\ \rho U_z \\ B_x \\ B_y \\ B_z \\ \rho e_t + p_G \\ 0 \end{pmatrix}, \quad \mathbf{P} = \begin{pmatrix} 0 \\ S_x p_G \\ S_y p_G \\ S_z p_G \\ -\overline{B}_f U_x \\ -\overline{B}_f U_y \\ -\overline{B}_f U_z \\ -\overline{B}_f (\mathbf{U} \cdot \mathbf{B}) \\ 0 \end{pmatrix}, \quad \Phi_{\mathbf{B}} = \begin{pmatrix} 0 \\ -B_x \overline{B}_f \\ -B_y \overline{B}_f \\ -B_z \overline{B}_f \\ S_x \Psi \\ S_y \Psi \\ S_z \Psi \\ 0 \\ c_h^2 \overline{B}_f \end{pmatrix}. \quad (15)$$

In Eq. (15) $p_G = p + B^2/2$ is the global pressure and $\overline{B}_f = (B_{f,L} + B_{f,R})/2$ is the magnetic flux. The variable Ψ is a scalar field and c_h is a numerical speed that allows us to convect the errors associated to $\nabla \cdot \mathbf{B} \neq 0$; both variables are related to the hyperbolic divergence cleaning technique, see [38] for more details. The PISO algorithm is a pressure-based method, which means that we need to calculate the thermodynamic pressure in a separated way:

$$p_f^n = \overline{\mathcal{P}}_5^+ p_L^n + \overline{\mathcal{P}}_5^- p_R^n. \quad (16)$$

In the prediction step the full system of equations (1)–(4) is solved in a segregated way. The first equation to be solved is an explicit version of the continuity equation, based on the mass flux m_f previously assembled with the AUSM-MHD method (Eqs. (14) and (15), first line). The solution of this equation gives a predicted value for density. Afterwards, an explicit equation for each component of the magnetic field is solved, with the magnetic fluxes calculated previously with

the AUSM-MHD method (Eqs. (14) and (15), fifth, sixth and seventh lines). The solution of Eq. (4) provides predicted values of B_x^* , B_y^* , and B_z^* . The Laplacian term (Eq. (7)) is calculated implicitly with a fully implicit Euler time-discretization, thus avoiding time-step restrictions that normally arise due to the different time scales between convection and diffusion terms. The predicted velocity field, \mathbf{U}^* , is obtained by solving the explicit momentum equations for each direction. The pressure gradient and the magnetic field terms are treated in an explicit way using the predicted magnetic field values B_x^* , B_y^* , B_z^* (from Eq. (4)) and the previously calculated face values of pressure, Eq. (16). The discretized momentum equation for \mathbf{U}^* is given by

$$a_p^U \mathbf{U}^* = \mathbf{H}(\mathbf{U}^n) - \nabla p_f^n, \quad (17)$$

where a_p^U is the central velocity coefficient and the operator $\mathbf{H}(\mathbf{U}^n)$ is built using the convective and diffusive terms of neighbour cells to P , the magnetic explicit terms and the explicit part of the time derivative:

$$\mathbf{H}(\mathbf{U}^n) = \sum a_N^U \mathbf{U}_N^n + S_B^* + \frac{\rho^* \mathbf{U}^n V_P}{\Delta t}, \quad (18)$$

where V_P is the geometrical volume of cell P . In order to remove time step restrictions, the second order viscous term is solved in an implicit way using Euler time discretization and a central differencing scheme is used for interpolation. The last equation to be solved, before the PISO correction cycle, is an equation for the total energy. Afterwards, the temperature field, T , is updated using the correspondent equation of state:

$$T^* = \frac{1}{c_v} \left[e_t^* - \frac{1}{2} \left\{ (\mathbf{U} \cdot \mathbf{U})^* + \frac{(\mathbf{B} \cdot \mathbf{B})^*}{\rho^*} \right\} \right]. \quad (19)$$

With the new temperature, new values for the compressibility coefficient are evaluated, $\psi^* = 1/RT^*$, and density can then be updated, $\rho^{**} = \psi^* p^n$.

3.1.2. Correction step

The $\mathbf{H}(\mathbf{U}^n)$ operator gives an intermediate velocity field which does not take into account the effect of pressure, refer to [30] for more details. Mach number interpolation functions are calculated once again inside the PISO loop, with the AUSM-MHD method. These new functions are applied to calculate the sonic flux to be used in the pressure equation:

$$F_s^* = c_f^* \left(\overline{\mathcal{M}}_4^+ \psi_L^* + \overline{\mathcal{M}}_4^- \psi_R^* \right). \quad (20)$$

The pressure equation is built and solved using the previously obtained values for compressibility, ψ^* , and density, ρ^{**} , as

$$\frac{\partial(\psi^* p^*)}{\partial t} + \nabla \cdot (F_s^* p^*) - \nabla \cdot \left(\frac{\rho^{**}}{a_p^U} \nabla p^* \right) = 0, \quad (21)$$

and gives the predicted value for the pressure, p^* . The velocity field is corrected in an explicit way using the new pressure gradient and the first predicted velocity. The pressure gradient is again calculated with the pressure face value

obtained using the interpolated Mach number functions:

$$\mathbf{U}^{**} = \frac{\mathbf{H}(\mathbf{U}^n) - \nabla p_f^*}{a_p^U}. \quad (22)$$

Finally, density is corrected using the equation of state $\rho^{***} = \psi^* p^*$. This cycle should be repeated until the continuity equation is satisfied and in all calculations we have applied two correction steps.

3.2. Thruster parameters

Several parameters are used to assess the performance of an MPD thruster. The overall thrust force is computed from the momentum flux at the thruster exit:

$$F = \int_{out} (\rho U^2 + p) dS. \quad (23)$$

Eq. (23) is similar to the one that is normally used for calculating the thrust in rocket engines. Note that an MPD is not an air-breathing propulsion system and that the propellant is stored on-board. The free-stream pressure is here neglected since the thruster exit is assumed to be on vacuum conditions. The electromagnetic (ELM) component of the total force is calculated with the volume integral of the axial component of the Lorentz force:

$$F_{ELM} = \int_V (\mathbf{j} \times \mathbf{B})_x dV. \quad (24)$$

The thermal contribution is easily obtained as the difference between total and ELM forces:

$$F_{Term} = F - F_{ELM}. \quad (25)$$

The specific impulse is a way of measuring the efficiency of a propulsion system:

$$I_{spec} = \frac{F}{\dot{m} g_0}, \quad (26)$$

where $g_0 = 9.8 \text{ m/s}^2$ is the acceleration of gravity. The efficiency of a two-dimensional nozzle can be obtained by the relation between the propulsion force and inlet parameters [39]:

$$\text{Eff.} = \frac{F^2}{2\dot{m} I(V + V_{elet})}, \quad (27)$$

where V is the electrical potential difference across the plasma, which can be obtained by the line integral of Ohm's law from anode to cathode:

$$V = \int \mathbf{E} \cdot d\mathbf{l} = \int (\eta \mathbf{j} - \mathbf{U} \times \mathbf{B}) \cdot d\mathbf{l}. \quad (28)$$

The potential drop due to electric sheath formation near the electrode walls was estimated to be $V_{elet} = 20 \text{ V}$ based on the experimental observations [21,40]. It is known that the potential drop due to electric sheath formation, when compared with the potential drop in the plasma, may assume a significant value, which will tend to decrease the efficiency of the nozzle. Therefore, assuming a constant value for V_{elet} could lead to an error in the performance computation. Nonetheless, the modeling of such phenomena is frequently discarded by several researchers [40] and the same will be done here. This needs to be taken into account in the results, since it will only allow for a

qualitative comparison between the performance of the several computed thrusters.

3.3. Real gas model

For the range of temperatures of a self-field MPD thruster the ideal gas model fails in the prediction of the thermodynamic variables. It is known that, for argon, the perfect gas approximation is not accurate for temperatures greater than 5000 K. Above this limit there is a huge discrepancy between the behavior of an ideal and real gas. For an ideal gas the inverse of compressibility is a linear function of temperature:

$$\psi^{-1} = RT, \tag{29}$$

where $R = k_B/M_i$ is the plasma constant that is obtained by the relation between the Boltzmann constant, k_B , and the mass of a particle of argon, M_i . The temperature slope given by Eq. (29) is not satisfactory and we have already remarked that the plasma transport properties are highly dependent on the temperature field; for example, in Eq. (8) the value of σ increases with $T^{3/2}$. This is a crucial point in plasma modeling, since an incorrect prediction of temperature can completely alter the character of the induction equation and of the remaining system of equations. It is therefore very important to include a real gas model into the MHD numerical method.

The real gas approximation that has been incorporated in the current numerical model is based on partition functions for argon [17]. This results in a particular function for compressibility ($T(K)$):

$$\begin{cases} \psi = \left(\frac{1}{R}\right) \frac{1}{T} & \text{if } T < 5000 \\ \psi = \frac{2K_2}{-K_1 + [K_1^2 - 4K_2(K_0 - T)]^{1/2}} & \text{if } 1^* \\ \psi = \frac{K_1}{T - K_0} & \text{if } 2^* \end{cases}, \tag{30}$$

with

$$\begin{aligned} 1^* & 5000 < T \leq 11\,498 \cup 14\,488 < T < 21\,688 \\ 2^* & 11\,498 < T \leq 14\,488 \cup T > 21\,688 \end{aligned}$$

Table 1
Coefficients for the calculation of ψ as a function of temperature [41].

Range for T (K)	K_0	K_1	K_2
$T \leq 11\,497.9$	0	0.00599	-7.18×10^{-10}
$11\,497.9 < T \leq 14\,488.3$	7935	0.00119	0
$14\,488.3 < T \leq 21\,687.7$	0	0.00317	-9.79×10^{-11}
$21\,687.7 < T \leq 29\,652.6$	12 460	0.00094	0
$T > 29\,652.6$	14 820	0.000811	0

Table 2
Coefficients for the calculation of γ as a function of temperature [41].

Range for T (K)	K_3	K_4	K_5	K_6
$8000 < T \leq 13\,000$	1.112166	0.529956	8050.606514	1318.851134
$13\,000 < T \leq 40\,000$	1.105401	0.025267	15142.82094	2394.061632

In Eq. (30) K_0 , K_1 and K_2 are coefficients that were calculated to replicate the data from [27], see Table 1. This model was incorporated by [41] in the framework of a density-based code and we have here adapted his formulation for inclusion on a pressure-based method [33].

The real gas adiabatic index is also calculated as a function of temperature:

$$\gamma(T) = K_3 + K_4 e^{-((T - K_5)/K_6)^2}, \tag{31}$$

where K_3 , K_4 , K_5 and K_6 are again function coefficients that were calculated to fit a particular mathematical function, see Table 2.

4. Numerical modeling of a 2D self-field MPD thruster

In this section the numerical method described in section 3 is applied for the computation of a two-dimensional self-field MPD thruster. This quasi-bidimensional experimental MPD setup was built by Toki et al. (see Fig. 1 in [42]) as a way of analysing and visualizing the plasma flow and current discharge pattern inside an MPD. This is normally prohibitive inside co-axial MPD thrusters due to the geometrical configuration of the discharge chamber. Here the usage of probes is the only solution available, but such measuring technique will also lead to unrealistic perturbations on the main flow. It is noted that a two-dimensional geometry does not fully reflect the physics of a co-axial MPD, however it is governed by the same physical principles and it is characterized by the same acceleration mechanisms. Therefore it can still provide the needed information for the development and validation of MPD numerical codes.

Regarding the numerical model the following assumptions were made with respect to the real model. The propellant gas is argon and we assume that it is injected in the discharge chamber in a state of total ionization. We can then assume that the plasma is treated as a single fluid, quasi-neutral in a state of thermal equilibrium ($T = T_e = T_i$, where e and i subscripts are related to electrons and ions, respectively). Several phenomena are neglected, namely viscosity; thermal conductivity; electrical sheath; Hall effect; and radiation processes. Electrical resistivity is given by Spitzer–Harm’s formulation, see Eq. (8). Also, the plasma flow is purely two-dimensional in the xy plane.

In the next subsection the MHD numerical model is validated for the computation of self-field MPD nozzles. Afterwards the influence of the geometrical configuration of the cathode and the anode is analysed. In Section 4.3 the effect of mass flow rate is computed. Finally, the inclusion of the real gas model in the developed code is assessed in Section 4.4.

4.1. Validation of the numerical model

For the purpose of validation, the MHD numerical model results for the FASC (Fig. 3(a)) configuration are compared against experimental [13] and numerical results from different sources [20,26]. The dimensions of the anode, cathode and numerical domain are shown in Fig. 4(a) top side. The cathode length is equal to 13 mm and the cathode

rounded tip is replaced by a sharp tip; for the remaining dimensions see Fig. 1(a).

4.1.1. Boundary conditions

Regarding boundary conditions, they are defined in the following way. At inlet, because of its subsonic regime, a mass flow rate of 2.5 g/s is prescribed. The phenomenon

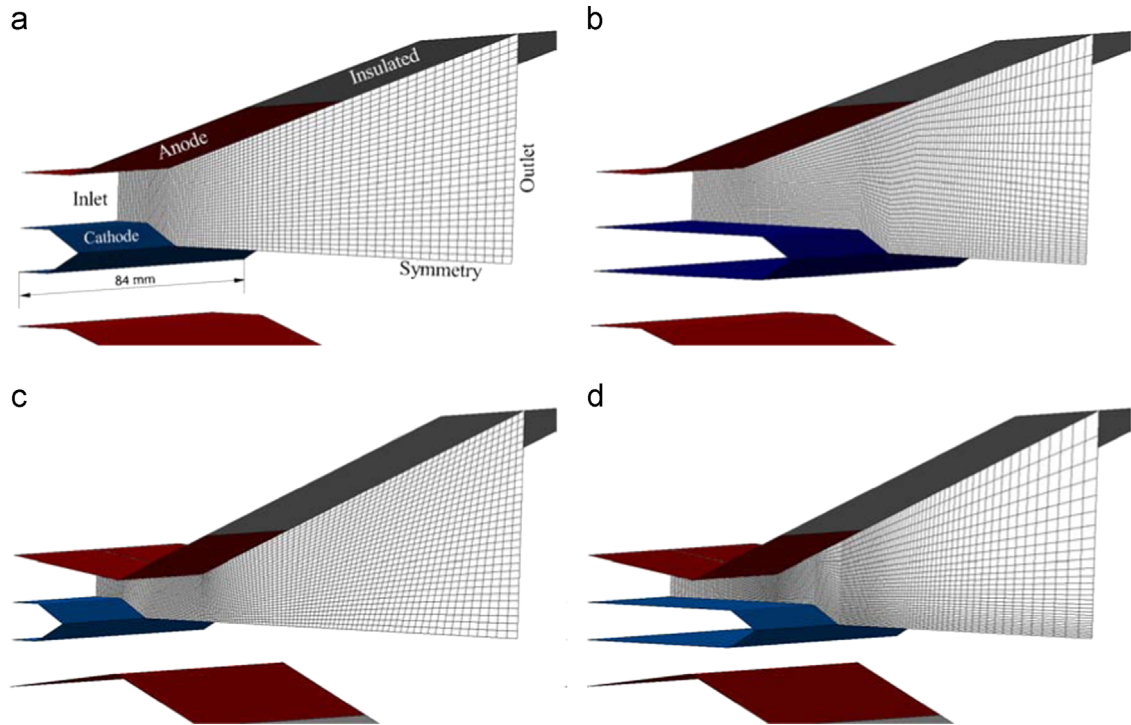


Fig. 3. Three-dimensional representation of the analysed configurations and respective grids. (a) FASC – flared anode short cathode (90×31 cells), (b) FALC – flared anode long cathode (132×31 cells), (c) CDASC – convergent divergent anode short cathode (126×31 cells), (d) CDALC – convergent divergent anode long cathode (134×31 cells).

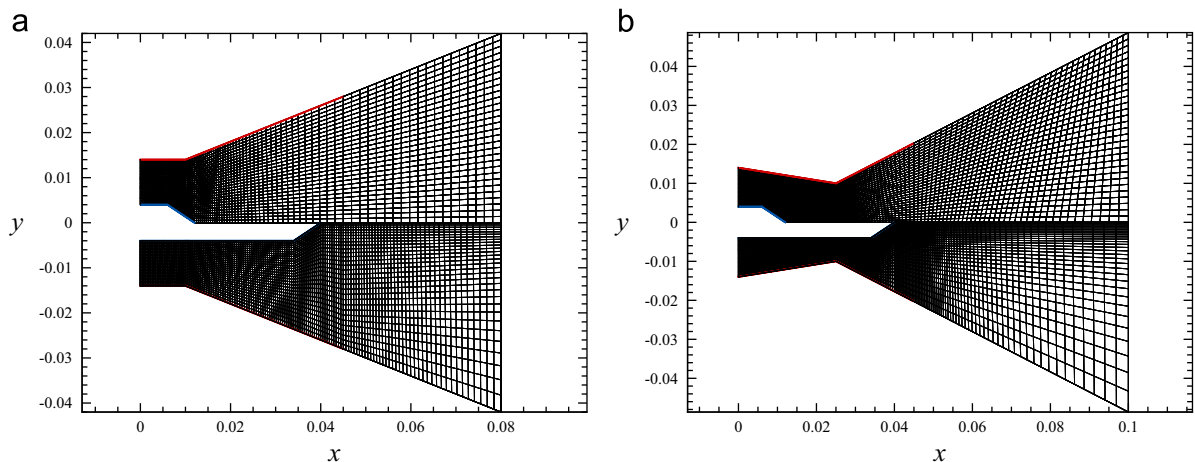


Fig. 4. Dimensions (in meters) of the numerical domain for the four analysed configurations. (a) Geometry with flared anode. (b) Geometry with convergent divergent anode. Note that for both anode configurations we have to only modify the cathode length, SC – short cathode (13 mm) and LC – long cathode (40 mm).

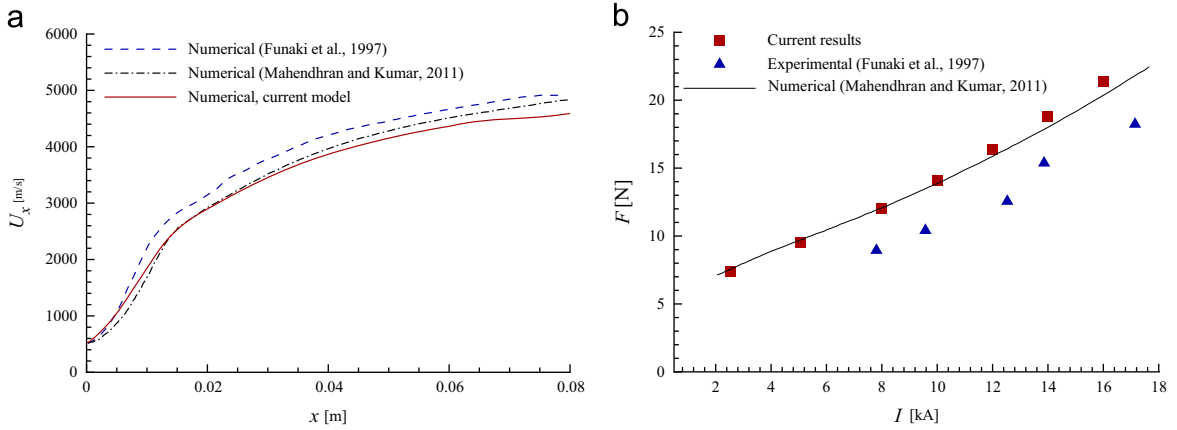


Fig. 5. Comparison between experimental and numerical results. (a) Velocity distribution computed along section a–a ($y = 0.009$ m) for the FASC configuration. (b) Numerical results and experimental data [20] for momentum thrust.

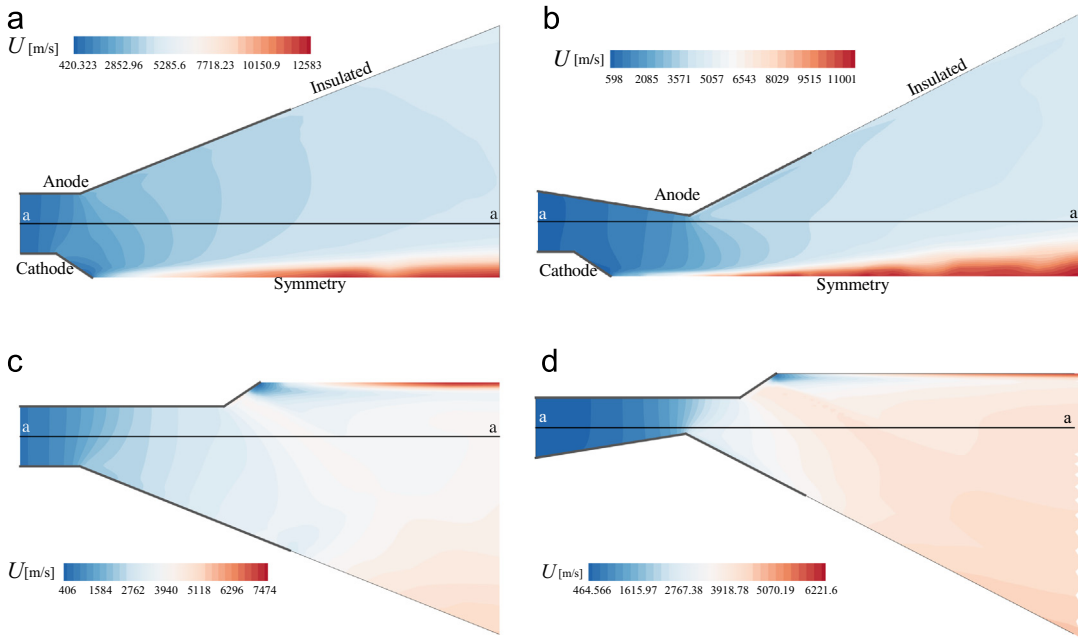


Fig. 6. Velocity magnitude contours computed for a discharge current of $I = 8000$ A and a mass flow rate of $\dot{m} = 2.5$ g/s. (a) FASC. (b) CDASC. (c) FALC. (d) CDALC.

associated to plasma ignition at the inlet is too much complex to be modeled and is here ignored. Instead a static temperature field of $T = 5000$ K is assumed and the highly ionized flow enters the chamber. At the outlet the flow is supersonic, which requires zero order extrapolation from the solution domain for all dependent variables. On all the electrodes and insulated walls a slip boundary condition is defined for velocity and an adiabatic condition is imposed for the thermodynamic variables. Regarding the electromagnetic boundary conditions they were prescribed in the following way. For the electrodes it is assumed that they are perfect conductors of electricity, and so the electrical resistivity on the wall is equal to zero. Such condition requires that the component of the electric current density tangential to the wall vanishes, therefore,

according to Ampère's law the tangential component of the magnetic field should be continuous on the electrode walls. The inlet value of the magnetic flux is calculated as a function of the discharge current:

$$B_0 = \frac{\mu_0 I}{2W}, \tag{32}$$

where I represents the discharge current and W is the thruster width, in this case $W = 84$ mm. In the perfect insulating wall and symmetry plane the magnetic flux density is set to zero. Fig. 5 shows a representation of the thruster discharge current and its interaction with the anode and insulating walls. One can observe that the induced magnetic field on the wall results from the two components of the electric current. Close to the anode

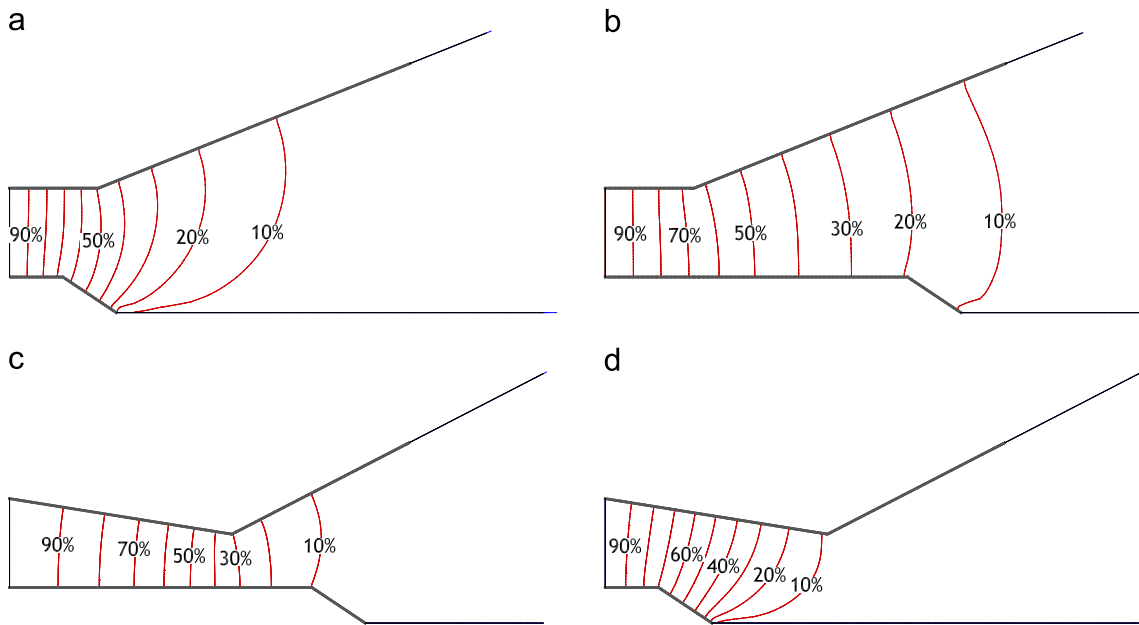


Fig. 7. Magnetic field distribution for a discharge current of 2500 A computed for all configurations: (a) FASC; (b) FALC; (c) CDALC; (d) CDASC. The isolines are represented in terms of percentage of inlet value.

wall, the net value of the electric current in the axial direction (J_x) is null because we have a positive and negative value of the current in the outlet cross section. Therefore, according to the Ampère theorem, the magnetic field due to the axial current is null when a small component due to the current perpendicular to the axis (J_y) induces a magnetic field at the vicinity of the anode. But considering the situation at the insulating wall where the electric current component perpendicular to the wall vanishes, the same reasoning leads to a zero value of the magnetic field, thus justifying the choice $B_z=0$ at the insulating wall.

4.1.2. Results

Fig. 2(a) shows the axial velocity distribution computed along section a–a ($y = 0.009$ m, see Fig. 6(a)), for an applied discharge current of $I = 8000$ A. For comparison the numerical results obtained by [20,26] are also plotted. One can observe that the computed velocity profiles agree very well with each other inside the discharge chamber, but the velocity here computed is slightly lower in the nozzle exit plane. A more realistic validation requires a direct comparison with experimental data. The plot in Fig. 2(b) shows a comparison between the computed and experimental results for the momentum thrust on the FASC configuration. It is seen that the present model over-predicts the propulsion force. Nevertheless, the trend is quite similar and when the solution is compared with the results obtained by others [26], who used a similar numerical model, we observe that our results agree very well. The over-prediction was expected since several physical aspects of plasma flow were neglected in the model formulation. However, the computed thrust follows the same trend of the experimental data as the discharge current increases, and this is a good indicator that the model is fulfilling its objectives.

4.2. Cathode and anode geometrical effects

In this section the effects of electrode geometry on the propulsion efficiency are analyzed. Fig. 3 shows a three-dimensional representation of the configurations analysed, while in Fig. 4 the dimensions of the different MPD nozzles are represented in a xy plot. The geometrical aspects that were addressed are the cathode length and the orientation of the anode. Regarding anode orientation a purely divergent (FA) and a convergent-divergent (CDA) configurations are computed. For the cathode length a short cathode (SC) with length equal to 13 mm and a long cathode (LC) with length equal to 40 mm are analysed for each anode type.

Regarding boundary conditions the same parameters of Section 4.1 are imposed, namely a mass flow rate of 2.5 g/s and a temperature of 5000 K are fixed at the inlet, and all the dependent variables are extrapolated from inside the solution domain at outlet. In the electrodes a perfectly electrical conducting boundary is specified.

Fig. 6 shows the contours plots of velocity magnitude for an imposed discharge current of $I = 8000$ A. The two SC configurations represented in Fig. 6(a) and (b) show similar values of velocity between them but, when compared with the LC configurations in (c) and (d), they show higher exhaust velocity. This behaviour is in agreement with the experimental results of [13].

The magnetic field distribution for a discharge current of $I = 2500$ A is shown in Fig. 7 in terms of percentage of the inlet value. The results obtained for the different configurations show that the field lines accumulate near the cathode tip due to its geometrical orientation. Such concentration of electric current will generate an increase of plasma acceleration due to joule heating effect. We note that the short cathode configurations are the ones that result in higher concentration of discharge current lines near the cathode tip. Indeed it has already been shown in

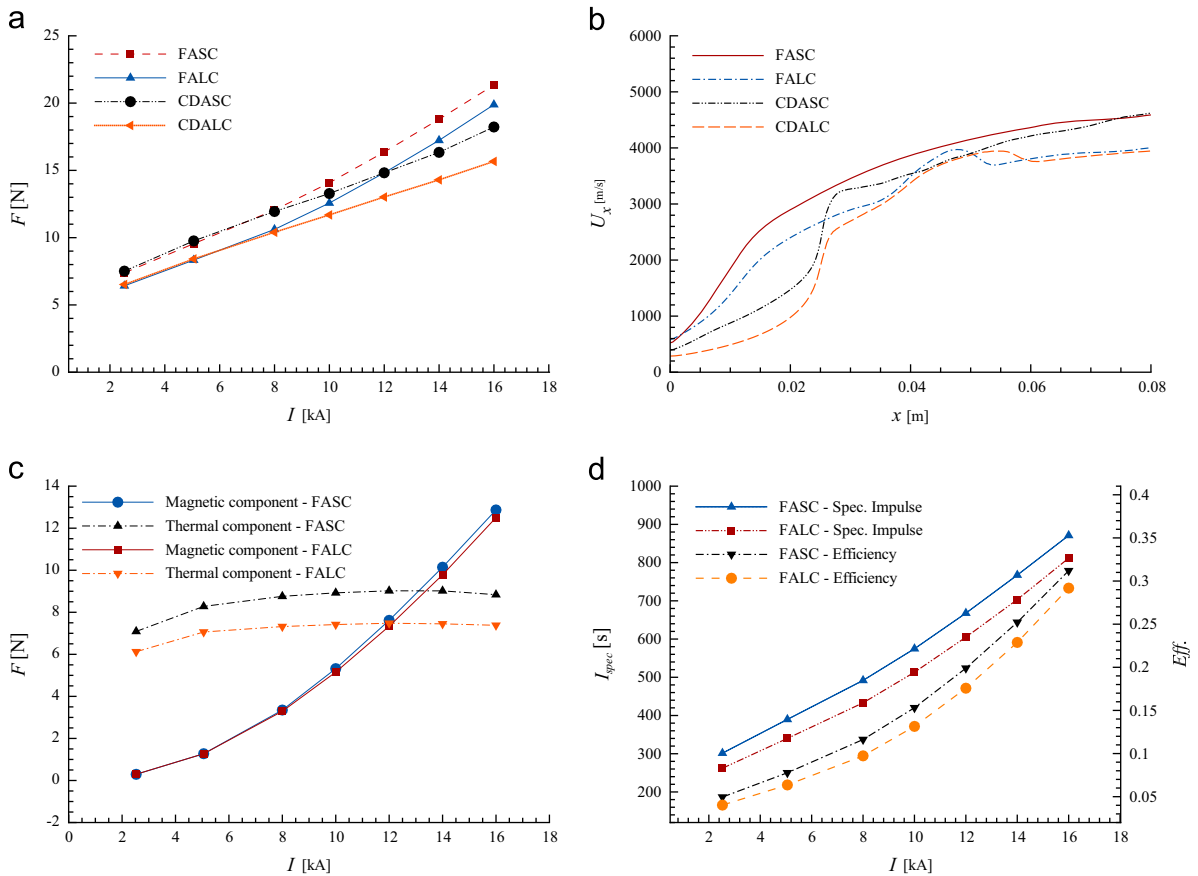


Fig. 8. (a) Thrust values computed for the several nozzle configurations as a function of discharge current. (b) Axial velocity profile computed along section a–a ($y=0.009$ m). (c) Electromagnetic and thermal components of thrust force computed on the FASC and FALC configurations. (d) Specific impulse and efficiency computed on the FASC and FALC configurations.

Fig. 6 that these are the configurations that achieve higher exhaust velocities.

Fig. 8(a) shows a comparison between the overall thrust values computed for each configuration as a function of the discharge current. We observe that the configurations with shorter cathode result in higher propulsion force for the entire range of discharge current. Note that the nozzles with a convergent-divergent anode, for discharge currents above $I=8$ kA, show lower values of propulsion. The axial velocity profile computed along section a–a ($y=0.009$ m) for each of the nozzles, and for a discharge current of 8000 A, is plotted on Fig. 8(b). As expected, the short cathode configurations produce higher values of axial velocity.

We analyse now separately the electromagnetic (Eq. (24)) and thermal (Eq. (25)) components of the thrust force for the FA configuration. Fig. 8(c) shows the evolution of these two propulsion mechanism as a function of the discharge current for both cathode lengths. The results show that for almost the entire range of discharge current the thermal thrust is superior to the electromagnetic thrust, and that the situation is reversed for a discharge current of $I \approx 13$ kA in the short cathode configuration, and $I \approx 12$ kA in the long cathode configuration. Fig. 8(c) also demonstrates that the superior thrust produced by the short cathode nozzle is solely related to an higher thermal contribution, since the electromagnetic thrust curves are almost coincident. In Fig. 8(d) the results for the specific

impulse (Eq. (26)) and efficiency (Eq. (27)) computed in the FASC and FALC geometries are plotted. As expected the FASC configuration shows higher specific impulse since, for the same mass of propellant and discharge current, it generates higher values of thrust, hence also resulting in a superior efficiency.

4.3. Variation of mass flow rate

In this section the effect of mass flow rate on the efficiency of the two FA geometries is analyzed. The results are obtained for a discharge current of $I=8000$ A and for an imposed inlet temperature $T=5000$ K. For the entire range of tested mass flow rates (0.5–2.5 g/s) the flow is subsonic at the inlet and supersonic at the outlet, thus we apply the same boundary conditions of the previous cases. In Fig. 9(a) the thrust components are plotted as a function of the mass flow rate. Once more it is the short cathode configuration that results in higher values of thrust. As expected the electromagnetic component is constant for the entire range of mass flow and the values computed in both geometries are almost coincident. On the other hand, the thermal component shows a linear growth as higher quantity of propellant is injected into the MPD nozzle. However the discrepancy between the SC and LC geometries is also increasing with the mass flow rate. Such behaviour should be related to the Joule heating effect since higher values of mass rate will allow higher absorption

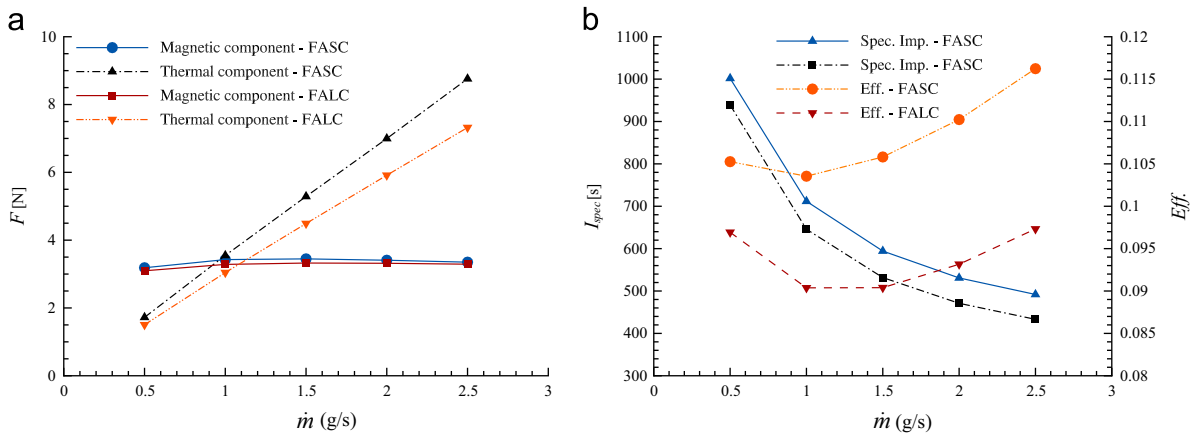


Fig. 9. (a) Magnetic and thermal components of thrust. (b) Specific impulse and efficiency obtained as a function of the mass flow rate on the FASC and FALC geometries.

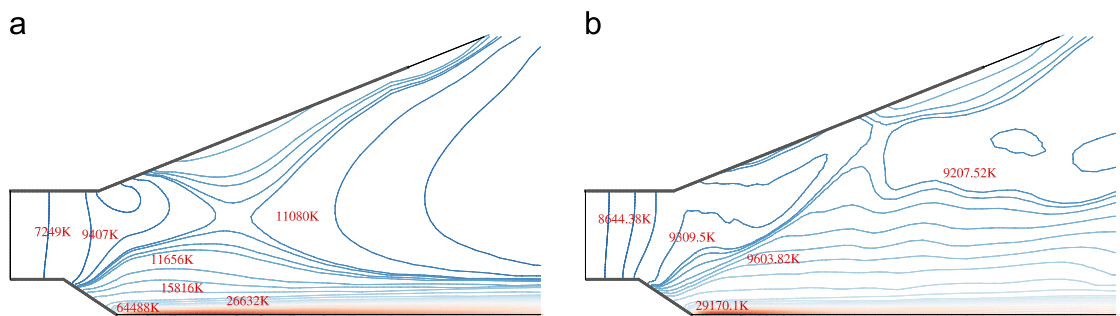


Fig. 10. Temperature contour plots using (a) an ideal gas equation; (b) with inclusion of the real gas model.

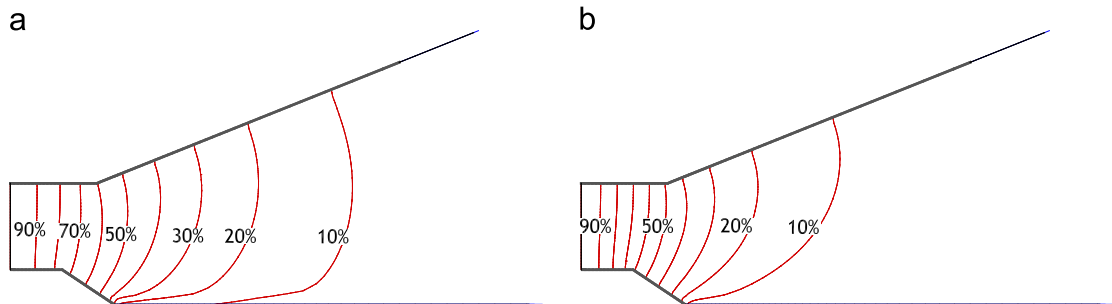


Fig. 11. Induced magnetic field distribution: (a) ideal gas equation; (b) real gas model.

of electrothermal energy. Fig. 9(b) shows the evolution of efficiency and specific impulse as the mass flow rate increases. It is observed that at the lower range of mass flow rates the nozzle produces higher values of specific impulse. Regarding efficiency, it is again the FASC configuration that performs better. The efficiency curves also show that, for the range of mass flow rate between 0.5 and 1 g/s, the performance decreases. During this interval, the dominant mechanism of acceleration is the electromagnetic one; for superior mass flow rates the flow is ruled by the electrothermal component of thrust. More investigation is therefore required in order to address what is the process behind this behaviour of efficiency. One can for example run the same problem for higher values of discharge current, which will allow to verify if the efficiency of the MPD decreases for the entire period of ELM

dominance, or if this behaviour is restricted to low values of mass flow rate.

4.4. Real gas model simulation

We look now into the effect of incorporating the real gas model in the current numerical method. Fig. 10(a) shows contour plots of temperature obtained with the ideal gas equation, at a discharge current of 5000 A. The temperature distribution computed with the real gas model, for the same value of discharge current, is shown in Fig. 10(b). It is clear that both models predict similar values of temperature inside the discharge chamber. However, near the cathode tip the ideal gas model predicts significantly higher values of T .

From Eq. (8) we know that the electrical conductivity increases with temperature. Thus, an over-prediction of temperature will also result in an incorrect distribution of \mathbf{B} . In Fig. 11 we show a comparison between the magnetic field distribution computed with the ideal (a) and the real (b) gas models. It is possible to observe that, inside the discharge chamber, the predicted solution is similar for both models. However, near the cathode tip the slope of the induced B_z is completely different. This is related to the higher values of electrical conductivity predicted by the ideal gas model, which will allow the magnetic field lines to be convected by the flow.

5. Conclusions

In the present work a mathematical model for the prediction of plasma flow on two-dimensional self-field MPD thrusters was presented and the related numerical method explained. The model is able to predict the two most important thrust mechanisms with some level of detail. Validation with experiments have shown that the proposed model gives the same trend of thrust growth as the discharge current increases, however with an over-prediction of force. This discrepancy is related to some of the model assumptions which do not account for several aspects of plasma physics.

The model is able to detect the geometrical influence of the electrodes on the electric current discharge pattern, which subsequently affect the efficiency of the MPD. We have verified that a reduction of cathode length can be beneficial in the analysed regime. The same behaviour was observed experimentally by others, hence meaning that the fundamental part of the code is fulfilling its objectives.

A real gas model was also included in the numerical formulation. We have shown that the real gas model allows us to compute a more realistic temperature distribution, which is going to influence the electrical conductivity and consequently the magnetic field distribution.

A mass flow rate study was also accomplished, for which we have verified that for the entire range of studied inflow mass flow rate the FASC configuration performed better than the FALC configuration. We have also shown that for a constant discharge current, the specific impulse is larger when the mass flow rate is smaller.

Future work will include more complex models of ionization and the inclusion of transport phenomena, namely plasma viscosity and thermal conductivity. The inclusion of multi-species models, specially for the internal energy of heavy species and electrons may also be very important for a correct prediction of temperature and transport variables.

Another important aspect is related to the possibility of calculating three-dimensional effects on MPD nozzles. It is known that an MPD nozzle working on off-project conditions may generate 3D flows, and that the position of the plasma injectors could be symmetrical or not. In this way for the design of MPD nozzles it is particularly important to develop a 3D computational model.

Acknowledgements

The present work was supported by Portuguese Foundation for Science and Technology (FCT) with Grant no. SFRH/BD/

60285/2009 and by FCT project PTDC/CTESPA/114163/2009 “SpaceProp – MHD Numerical Modeling in nozzles of MPD Thrusters for Space Propulsion”. Additional financial support was provided by C-MAST – Center for Mechanical and Aerospace Sciences and Technologies, Research Unit No. 151. The authors would like to thank the reviewers for their comments which helped to improve the paper, and are particularly indebted to Prof. Alemany (CNRS - Centre National de la Recherche Scientifique, University of Grenoble) for his clarifying comments on the imposition of the magnetic boundary condition on the insulating wall.

References

- [1] V.P. Chiravalle, *Acta Astronaut.* 62 (2008) 374–390.
- [2] L. Johnson, M. Meyer, B. Palaszewski, D. Coote, D. Goebel, H. White, *Acta Astronaut.* 82 (2013) 148–152. 7th [IAA] Symposium on Realistic Advanced Scientific Space Missions Aosta, Italy, July 2011.
- [3] M. Coletti, *Acta Astronaut.* 81 (2012) 667–674.
- [4] F. Guarducci, G. Paccani, J. Lehnert, *Acta Astronaut.* 68 (2011) 904–914.
- [5] M. Auweter-Kurtz, H. Kurtz, in: 4th International Spacecraft Propulsion Conference (ESA SP-555), Chia Laguna, Italy.
- [6] J.M.G. Chanty, Analysis of two-dimensional flows in magnetodynamic plasma , accelerators (Ph.D. thesis), Massachusetts Institute of Technology, 1992.
- [7] M.R. LaPointe, P.G. Mikellides, in: 37th Joint Propulsion Conference and Exhibit, AIAA-2001-3499.
- [8] D. Haag, M. Auweter-Kurtz, M. Fertig, in: Proceedings of 30th International Electric Propulsion Conference, IEPC-2007-138, Florence, Italy.
- [9] A. Kodys, E. Choueiri, in: AIAA 41st Joint Propulsion Conference, AIAA-2005-4247.
- [10] R. Tikhonov, S. Semenikhin, J. Brophy, J. Polk, in: 25th International Electric Propulsion Conference, IEPC-97-120.
- [11] H. Sato, K. Kubota, I. Funaki, in: 32nd International Electric Propulsion Conference, IEPC-11-258, Wiesbaden, Germany.
- [12] M.R. LaPointe, Numerical Simulation of Geometric Scale Effects in Cylindrical Self-Field MPD Thrusters, Technical Report CR-189224, NASA Lewis Research Centre, 1992.
- [13] I. Funaki, K. Kuriki, K. Toki, *J. Propuls. Power* 14 (1998) 1043–1048.
- [14] P.G. Mikellides, P.J. Turchi, N.F. Roderick, *J. Propuls. Power* 16 (5) (2000) 887–893.
- [15] P.C. Sleziona, M. Auweter-Kurtz, H.O. Schrade, in: Proceedings of 23rd International Electric Propulsion Conference, IEPC-93-066, Seattle.
- [16] T. Miyasaka, T. Fujiwara, in: Joint Propulsion Conferences, American Institute of Aeronautics and Astronautics, 1999.
- [17] K. Sankaran, E.Y. Choueiri, S.C. Jardin, *J. Propuls. Power* 21 (2005) 129–138.
- [18] B.L. England, P.G. Mikellides, in: Proceedings of 29th International Electric Propulsion Conference, IEPC-2005-206, Princeton.
- [19] P.G. Mikellides, B. England, J.H. Gilland, *Plasma Sour. Sci. Technol.* 18 (2009) 015002.
- [20] I. Funaki, K. Toki, K. Kuriki, *J. Propuls. Power* 13 (1997) 789–795.
- [21] K. Kubota, I. Funaki, Y. Okuno, in: 30th International Electric Propulsion Conference, IEPC-07-87, Florence, Italy.
- [22] P. Norgaard, E. Choueiri, in: 29th International Electric Propulsion Conference, IEPC-2005-006, Princeton University.
- [23] P. Sleziona, M. Auweter-Kurtz, H. Schrade, in: Proceedings of 20th International Electric Propulsion Physics Conference, IEPS-88-043, Garmisch-Partenkirchen.
- [24] R.M. Myers, M.A. Manteniaks, M.R. Lapointe, MPD Thruster Technology, Technical Report NASA-TM-105242, NASA Glenn Research Center, 1991.
- [25] K. Sankaran, L. Martinelli, S.C. Jardin, E.Y. Choueiri, *Int. J. Numer. Methods Eng.* 53 (2002) 1415–1432.
- [26] M. Mahendhran, A. Kumar, in: 32nd International Electric Propulsion Conference, IEPC-2011-228, Wiesbaden, Germany.
- [27] W.M. Sparks, D. Fischel, Partition Functions and Equations of State in Plasmas, NASA, Goddard Space Flight Center, 1971.
- [28] K. Sankaran, Simulation of plasma flows in self-field Lorentz force accelerators (Ph.D. thesis), Princeton University, 2005.
- [29] S. Han, J. Lee, K. Kim, *AIAA J.* 47 (2009) 970–981.
- [30] C.M. Xisto, J.C. Páscoa, P.J. Oliveira, D.A. Nicolini, *Int. J. Numer. Methods Fluids* 70 (8) (2012) 961–976.

- [31] T. Ogino, Y. Kajiwara, M. Nakao, K. Park, K. Fukazawa, Y. Yi, *Acta Astronaut.* 61 (2007) 923–931.
- [32] H. Goedbloed, Poedts, *Principles of Magnetohydrodynamics With Applications to Laboratory and Astrophysical Plasmas*, Cambridge University Press, Cambridge, 2004.
- [33] C.M. Xisto, J.C. Páscoa, P.J. Oliveira, *Int. J. Numer. Methods Fluids* 72 (11) (2013) 1165–1182.
- [34] C.M. Xisto, J. Páscoa, P.J. Oliveira, *J. Comput. Phys.* 275 (2014) 323–345.
- [35] R.I. Issa, *J. Comput. Phys.* 62 (1986) 40–65.
- [36] K.H. Kim, J.H. Lee, O.H. Rho, *Comput. Fluids* 27 (1998) 311–346.
- [37] M.A. Alves, P.J. Oliveira, F.T. Pinho, *Int. J. Numer. Methods Fluids* 41 (2003) 47–75.
- [38] A. Dedner, F. Kemm, D. Kröner, C.-D. Munz, T. Schnitzer, M. Wesenberg, *J. Comput. Phys.* 175 (2002) 645–673.
- [39] K. Kubota, I. Funaki, Y. Okuno, in: 31st International Electric Propulsion Conference, IEPC-2009-227.
- [40] K. Kubota, I. Funaki, Y. Okuno, *IEEE Trans. Plasma Sci.* 37 (2009) 2390–2398.
- [41] K. Sankaran, Simulation of MPD flows using a flux-limited numerical method for the MHD equations (Master's thesis), Princeton University, 2001.
- [42] K. Toki, M. Sumida, K. Kuriki, *J. Propuls. Power* 8 (1992) 93–97.